MNRAS **000**, 1–9 (2016) Preprint 5 April 2024 Compiled using MNRAS LATEX style file v3.0

Fast launch speeds in radio flares, from a new determination of the intrinsic motions of SS 433's jet bolides

Robert M. Jeffrey[1], Katherine M. Blundell[1], Sergei A. Trushkin[2,3], and Amy J. Mioduszewski[4]

[1]*University of Oxford, Department of Physics, Keble Road, Oxford, OX1 3RH, U.K.*
[2]*Special Astrophysical Observatory RAS, Karachaevo-Cherkassian Republic, Nizhnij Arkhyz, 36916, Russian Federation*
[3]*Kazan Federal University, Kazan, 420008, Russian Federation*
[4]*NRAO, P.O. Box 2, Socorro, NM 87801, USA*

Accepted XXX. Received YYY; in original form ZZZ

ABSTRACT

We present new high-resolution, multi-epoch, VLBA radio images of the Galactic microquasar SS 433. We are able to observe plasma knots in the milliarcsecond-scale jets more than 50 days after their launch. This unprecedented baseline in time allows us to determine the bulk launch speed of the radio-emitting plasma during a radio flare, using a new method which we present here, and which is completely independent of optical spectroscopy. We also apply this method to an earlier sequence of 39 short daily VLBA observations, which cover a period in which SS 433 moved from quiescence into a flare. In both datasets we find, for the first time at radio wavebands, clear evidence that the launch speeds of the milliarcsecond-scale jets rise as high as $0.32c$ during flaring episodes. By comparing these images of SS 433 with photometric radio monitoring from the RATAN telescope, we explore further properties of these radio flares.

Key words: stars: individual: SS 433 – stars: jets – ISM: jets and outflows – accretion, accretion discs

1 INTRODUCTION

Over almost 40 years, astronomers have continued to be surprised by the variety of phenomena displayed by the Galactic microquasar SS 433's binary system and outflows. It is one of the few known microquasars whose relativistic jets have been persistently resolved both in space and in time, allowing us to probe their evolution. In arcsecond-scale radio images, the precessing jets manifest themselves in a distinctive distorted corkscrew shape (Blundell & Bowler (2004)), while propagating ballistically away from the launch point at approximately 8 mas d^{-1}. Using the VLA, the jet plasma is observable over $\sim$ 18 months after launch. At milliarcsecond-scales, the jet can be resolved, and individual pairs of antiparallel discrete plasma ejections (often referred to as bolides) can be tracked for about 30 days. The jet also appears as distinctive moving emission lines in optical (Margon et al. (1979)) and X-ray (Marshall et al. (2002)) spectra.

Both the spectral behaviour and the morphology of the radio emission are fairly well described by the precessing jet model of Abell & Margon (1979) and Hjellming & Johnston (1981). In this "kinematic model", antiparallel jets of plasma are symmetrically launched at $0.26c$ along a precessing ejection vector, which traces out a cone in space every 163 days (see Eikenberry et al. (2001) for parameter fits from optical spectroscopy). Superimposed on this, the jet axis displays small, regular nutations with periodicity of 6 days (Katz et al. (1982)).

The kinematic model is not, however, the complete picture. It describes the average behaviour of the jets, which have shown a remarkable persistance and stablity over a few decades of optical spectroscopy (e.g. Margon & Anderson (1989), Eikenberry et al. (2001), Blundell & Bowler (2005), Clark et al. (2007)). But, both in the arcsecond-scale radio jets (Blundell & Bowler (2004)) and in the optical spectra (Blundell & Bowler (2005), Blundell et al. (2007)), there is clear evidence that the jet speed varies over timescales as short as a few days. The distribution of launch speeds peaks at roughly the mean value, $0.26c$, and spreads beyond the range from $0.2c$ to $0.3c$ (Blundell & Bowler (2005)).

The microquasar's brightness also displays variability in both optical and radio wavebands. At times, SS 433 enters an active state, in which its radio brightness may rise by between 50 and 100 per cent or more. It can remain in this state for as long as 90 days (Fabrika (2004)). Contemporaneous optical and radio observations of a flare in 2004 (Blundell et al. (2011)) revealed the coupled, multi-wavelength behaviour of the flaring phenomenon, and fit with a picture in which flares comprise enhanced mass loss through faster winds, faster launch speeds for the optical jet bolides, and a 2-part radio flare arising first from the wind, and then from the appearance of jet bolides. In particular, from archival radio and

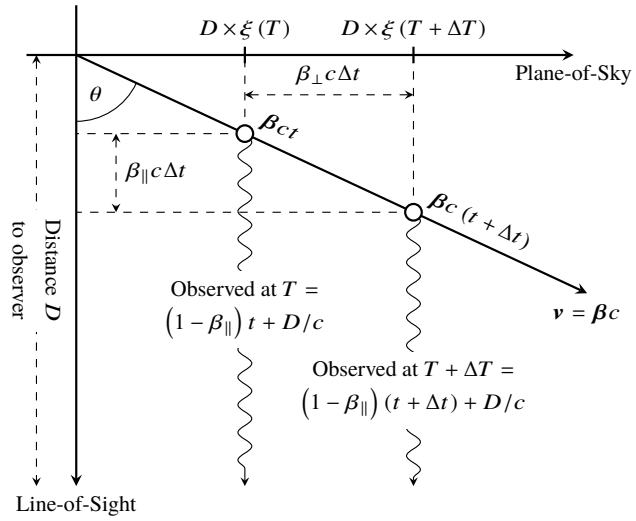

Figure 1. Schematic showing the role of light travel time effects in determining proper motions. It shows light pulses leaving a source that moves at $\boldsymbol{v} = \boldsymbol{\beta} c$ to be observed by a distant ($D \gg \beta c \Delta t$) astronomer on Earth. The events corresponding to emission of a light pulse occur at *coordinate* times t and $t + \Delta t$ in the observer's rest frame, while the events corresponding to those pulses reaching Earth occur at coordinate times T and $T + \Delta T$ respectively. From the geometry shown here, the time steps are related by $\Delta T/\Delta t = \left(1 - \beta_\parallel\right)$, since the second ray has to travel a shorter distance from position at emission to observation on Earth. At these two observations, the source's angular displacements from the core are $\xi\,(T)$ and $\xi\,(T + \Delta T)$. The proper motion measured by the astronomer on Earth is $\mu = \left[\xi\,(T + \Delta T) - \xi\,(T)\right]/\Delta T$, where $\xi\,(T + \Delta T) - \xi\,(T) = \beta_\perp c \Delta t / D$. By eliminating Δt, Equation 1 follows simply.

optical spectroscopic data, Blundell et al. (2011) report that faster optical jets always precede radio flares by a couple of days.

In this paper, we outline a method for the determination of jet speed using spatially– and temporally–resolved radio maps. Using VLBA data from 2011-12 (Section 3) and 2003 (Section 4), we give the first unique determination of the speeds of SS 433's radio bolides on milliarcsecond scales. Finally, we discuss the relationship between bolide luminosity and speed in the context of flaring episodes.

2 CALCULATING JET BULK SPEEDS

2.1 Proper motions and line-of-sight velocities

Due to the finite travel time of light signals, the proper motion, μ, of a light source across the sky is given by:

$$\mu = \frac{\mathrm{d}\xi}{\mathrm{d}T} = \frac{\beta_{\mathrm{apparent}} c}{D} = \frac{c}{D}\frac{\beta \sin\theta}{1 - \beta\cos\theta} \tag{1}$$

where D is the distance to the source, c is the speed of light, θ is the angle of the source's intrinsic velocity to line-of-sight, and $v = \beta c$ is its speed. ξ is the angular displacement on the sky, and T denotes time passed according to the observer's clock (the epoch of observation) (see Figure 1 or, c.f., Longair (2011) for derivation).

Consider a pair of symmetric, antiparallel, ballistic jets, launched from a common core, both travelling at speed β, with the jet and counterjet aligned at angles θ and $\pi - \theta$ to the line-of-sight. Inserting these into the definition of proper motion, we can extract (e.g. Mirabel & Rodríguez (1994)) the line-of-sight velocity component, $\beta\cos\theta$:

$$\beta_\parallel = \beta\cos\theta = \frac{\mu_{\mathrm{jet}} - \mu_{\mathrm{cjt}}}{\mu_{\mathrm{jet}} + \mu_{\mathrm{cjt}}} = \frac{\xi_{\mathrm{jet}} - \xi_{\mathrm{cjt}}}{\xi_{\mathrm{jet}} + \xi_{\mathrm{cjt}}} \tag{2}$$

where μ_{jet} and μ_{cjt} denote the proper motions of the jet and counterjet respectively. The final equality follows from the assumptions of ballistic motion and simultaneous launch, where $\xi_{\mathrm{jet}} = \mu_{\mathrm{jet}}\Delta T$ and $\xi_{\mathrm{cjt}} = \mu_{\mathrm{cjt}}\Delta T$ are the angular displacements from the launch point observed at the same epoch (according to the observatory clock), ΔT after their simultaneous launch.

2.2 Launch epoch and intrinsic jet speed

For ballistically moving ejecta, it is now possible to extract both the launch epoch, T_{launch}, and the intrinsic speed, β. To find the launch epoch, we simply extrapolate back to the date on which the separation between jet and counterjet ejections was zero. Given two observations at epochs T and $T + \Delta T$, and defining the total angular separation $\xi_{\mathrm{tot}}\,(T) := \xi_{\mathrm{jet}}\,(T) + \xi_{\mathrm{cjt}}\,(T)$, we find:

$$T_{\mathrm{launch}} = T - \frac{\xi_{\mathrm{tot}}\,(T)}{\xi_{\mathrm{tot}}\,(T + \Delta T) - \xi_{\mathrm{tot}}\,(T)}\,\Delta T\,. \tag{3}$$

The quantity ξ_{tot} has the advantage that it is just the angular separation between the jet and counterjet bolides, and so can be determined independently of the absolute location of the centre. This is particularly useful for self-calibrated interferometric maps of SS 433, where the precise core location can be hard to identify.

Similarly, we can define a total proper motion $\mu_{\mathrm{tot}}\,(T) := \mu_{\mathrm{jet}}\,(T) + \mu_{\mathrm{cjt}}\,(T)$ as the rate at which the two bolides move apart. Using Equation 1, this total proper motion can be written:

$$\mu_{\mathrm{tot}} = \frac{\xi_{\mathrm{tot}}\,(T)}{T - T_{\mathrm{launch}}} = \frac{2c}{D}\frac{\beta_\perp}{1 - \beta_\parallel^2} \tag{4}$$

where $\beta_\perp = \beta\sin\theta$.

We can rearrange Equation 4 to find the velocity component perpendicular to the line-of-sight, $\beta_\perp$. Then, the jet speed itself can be written in terms of the total proper motion, μ_{tot}, and the line-of-sight velocity component, $\beta_\parallel$:

$$\beta = \sqrt{\beta_\perp^2 + \beta_\parallel^2} = \sqrt{\left[(D/2c)\,\mu_{\mathrm{tot}}\left(1 - \beta_\parallel^2\right)\right]^2 + \beta_\parallel^2} \tag{5}$$

where the line-of-sight velocity component, $\beta_\parallel$ is calculated using Equation 2.

3 2011-12 VLBA OBSERVATIONS

SS 433 was observed with the Very Long Baseline Array (VLBA) on MJD 55919.83 and MJD 55954.75 (i.e. on 2011-Dec-24, and 35 days later on 2012-Jan-28)[1]. These images are shown in Figure 2. These were *L*-Band observations at 1.6 GHz, giving a beam size of approximately 10 mas × 5 mas. The low frequency end of the band was grossly affected by radio frequency interference (RFI) and flagged. This gave us 6 contiguously spaced IFs of 16 MHz. After *a priori* amplitude and bandpass calibration, and fringe fitting to calibrate phase, these IFs were averaged down to a single channel, giving an image of the continuum for each epoch.

[1] Modified Julian Date (MJD) is days since midnight on 1858-Nov-17. This is JD - 2400000.5.

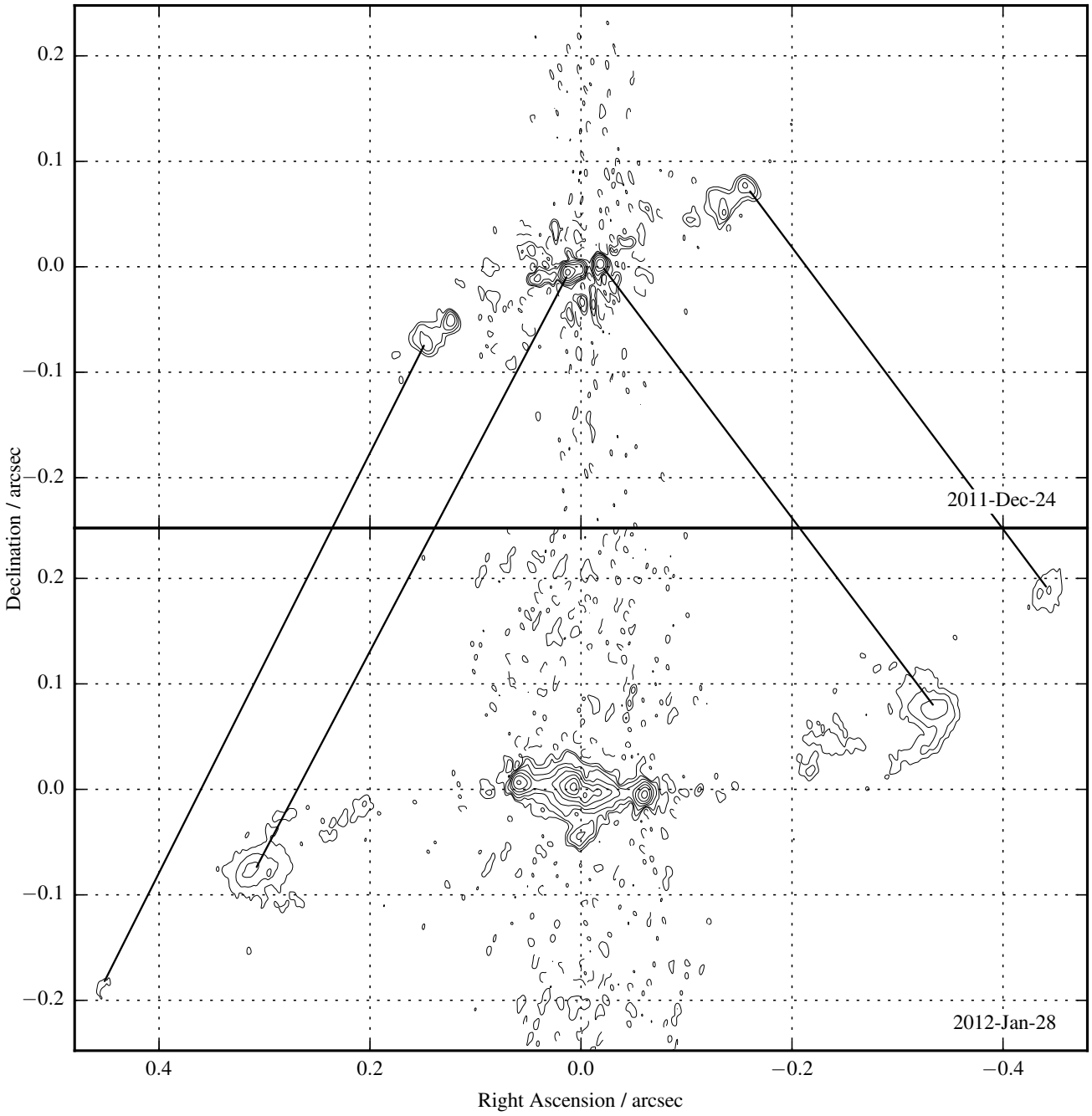

Figure 2. VLBA Observations of SS 433 in 2011-12. Contour levels are at 2^n times the minimum contour level, which is 2.2 mJy beam^{-1} in the upper panel, and 0.22 mJy beam^{-1} in the lower panel. One negative contour (dashed) at −1 times the minimum contour level is also shown. The connecting lines identify the same ejections across the two epochs.

Bolide	2011-Dec-24			2012-Jan-28			$T_{\rm launch}$	Line-of-Sight		Bulk Speed
	$\xi_{\rm jet}$	$\xi_{\rm cjt}$	$\xi_{\rm tot}$	$\xi_{\rm jet}$	$\xi_{\rm cjt}$	$\xi_{\rm tot}$	(MJD)	Velocity $\beta_\parallel = v_\parallel/c$		$\beta = v/c$
A	162.2	173.9	336.1	488.9	480.5	969.4	55901.3 ± 0.9	0.009 ±	0.029	0.288 ± 0.017
B	12.7	18.7	31.2	318.3	343.8	662.0	55918.1 ± 0.6	−0.039 ±	0.043	0.289 ± 0.017

Table 1. Angular displacements and derived launch dates, line-of-sight velocities, and launch speeds for bolides A and B in the 2011-12 observations. Angular displacements are given in milliarcseconds from the core (located at the origin of Figure 2). Speeds are given in units of c.

The data were flagged, calibrated, and imaged using standard routines in the AIPS software package (Greisen (2003)), following the recipes in Appendix C of the AIPS Cookbook (NRAO (1990)). Each 11 hour observation consisted of alternating 7 minute scans of SS 433, and 2 minute scans of the phase calibrator J1929+0507 (4° from the science target). The source rises and sets at different times at each antenna, and it was found that the images were improved by using only the middle 8 hours of each epoch, when the array coverage is fullest. To handle the complex, extended structure present in the jets, we found it to be essential to use the multi-scale implementation of CLEAN available within the AIPS task `IMAGR` (Greisen et al. (2009)). We found the greatest success when using 2 CLEAN scales, at 1 and 5 times the beam size.

A significant challenge in imaging arises because of time variation in SS 433, and especially from the motion of the jet bolides during the course of the observations. The length of our observations give us sufficient signal-to-noise to image the expanded jet bolides over an unparalleled period after launch. But, with proper motions of $\sim 8\,\mathrm{mas\,d^{-1}}$ and observations lasting almost half a day, the bolides move by almost a full beam in the course of the observations, violating the assumptions underlying the use of the Fourier transform in synthesis imaging. This is the principal cause of the spurious signals North and South of the main jet axis. Attempts to mitigate this by imaging subsections of the full scan were only partially successful. Nonetheless, the images we obtained are of sufficient quality for us to determine the locations of the jet bolides securely. In each figure, the lowest contour level is set at $\gtrsim 5\sigma$, where σ is the rms background noise away from the artefacts north and south of the jet. Accordingly, we are able to confidently locate even the faint outer bolides in the second epoch.

These two images show the milliarcsecond-scale jets of SS 433 in greater detail and over greater extent than any previous VLBI image of the system. We can trace the ejecta as they travel over $\gtrsim 0.4$ arcseconds on either side of the core, or $\gtrsim 50$ days from their initial launch, given that proper motions are of order of $8\,\mathrm{mas\,d^{-1}}$. In each epoch, we can identify a succession of pairs of bolides arising from antiparallel ejections of knots of jet plasma. The time-spacing of the two epochs is such that plasma that is launched shortly before the first observation has not had time to fade before the second, revealing for the first time the remarkable degree to which the jet knots expand as they fade (the implications of which will be discussed in a forthcoming paper (Jeffrey et al. in prep)).

For the two ejection complexes identified in both epochs, we can measure their angular displacements from an estimated core position, located at the origin in Figure 2. Then, we evaluate line-of-sight velocity, launch date, and jet bulk speed using Equations 2, 3, and 5 respectively.

The resulting values are given in Table 1. The two ejections occur on MJD 55901.3 ± 0.9 and MJD 55918.1 ± 0.6 (i.e., 18.5 ± 0.9 and 1.7 ± 0.6 days before the first observation). Both ejections launch bolides at speeds of almost $0.29c$. This is the first unique measurement of the bulk speeds of the radio jets on milliarcsecond scales. It is particularly noteworthy that the speeds lie at the upper end of the range of those fitted to the arcsecond-scale radio jets in Blundell & Bowler (2004), and also that they match the high optical jet speeds that Blundell et al. (2011) reported as being associated with flaring behaviour. We will discuss this further in Section 5.

4 ARCHIVAL VLBA OBSERVATIONS - THE SS 433 MOVIE

We can also apply the methods derived in Section 2 to historic VLBA observations of SS 433 in 2003.

SS 433 was observed on 39 out of the 42 days between 2003-June-26 and 2003-August-06, using 2 hour observation tracks with the VLBA at 1.4 GHz (*L*-Band). The data were reduced by one of the authors (AJM) with the AIPS software using standard techniques for VLBI imaging (as discussed in the AIPS Cookbook). Multiscale CLEAN was used to assist with imaging, as was careful boxing, guided by the predicted jet loci generated from the kinematic model. A movie of the colour-scale images from this campaign has previously been released to the community (`http://www.nrao.edu/pr/2004/ss433/`; Mioduszewski et al. (2004)). The individual observations are plotted as contour maps in Figure 3, and an animated version of these contour plots is available with the online Journal.

From a qualitative inspection of Figure 3, we can see that the jet consists mainly of a series of discrete ejection pairs, which we are able to track over multiple successive days' observing as they travel away from the core in an apparently ballistic fashion. In each case, both components of a pair of bolides appear to be launched simultaneously. In the first observation, 2 bolide pairs can be distinguished. Over the course of the 6 week campaign, a further 8 pairs are launched.

Throughout the campaign, the jet shows deviations from the kinematic model predictions (i.e. the crosses in Figure 3, using the parameter fits of Eikenberry et al. (2001)), implying variations in launch angle or in jet speed (or in both) that are not described by this simple model. Schillemat et al. (2004) noted that the proper motions deviate from those predicted by the model. In Section 4.1 below, we apply Equation 5 to show how these correspond to variations in the physical jet launch speed.

It is also interesting to note that SS 433's behaviour over the course of the 2003 campaign appears to be divided into two distinct phases. During the first part of the campaign, we observe a period of relative quiescence. Discrete jet ejections can be identified, but they have low luminosities relative to later bolides, and appear to lie within a more continuous background jet flow.

From about day 19 (i.e. from 2003-Jul-14, MJD 52834) until the end of the observing campaign, the jet appears to move to a more active phase featuring more intense bolide ejections. The jet appears more fragmented, with more pronounced gaps in the jet flow between individual ejections (note that all frames of Figure 3 are contoured at the same levels). This fragmentation suggests that the continuous jet seen in earlier epochs is actually disrupted, although it may be a dynamic range or *uv*-plane sampling effect.

We believe this second phase of behaviour to be the milliarcsecond-scale manifestation of a radio flare, and in Section 5 we will discuss this hypothesis in relation to existing observations of SS 433.

4.1 Proper motion analysis of the 2003 data

We can determine the bulk launch speeds of the individual jet ejecta by using the analysis of Section 2. The peak positions of individual bolides were determined using the AIPS task `JMFIT`. At each epoch, a single Gaussian component was fitted to each bolide; the peak positions of these Gaussians served as the bolide locations. These fits are available in machine-readable format with the online Journal.

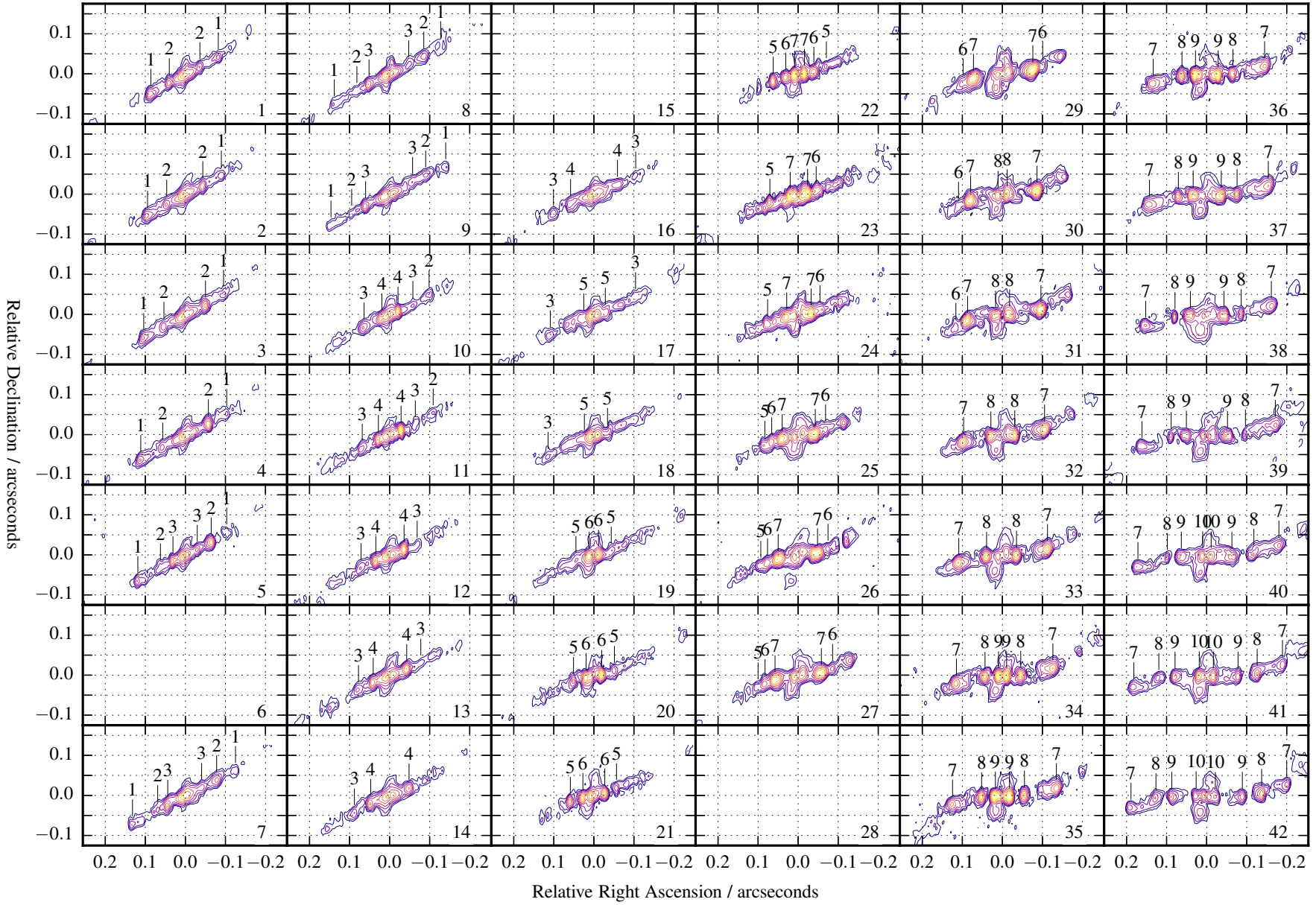

Figure 3. Contour Maps showing 2003 VLBA Observations of SS 433. Contour levels are identical across all frames, set at $2^n \times 0.7$ mJy beam^{-1} for integer n. The frame number corresponds to number of days from 2003-June-25 (i.e. MJD − 52815.0). The crosses denote the Kinematic Model predictions for bolides launched at 5 day intervals.

Next, we determine the proper motions, $\mu_{\rm jet}$ and $\mu_{\rm cjt}$, of the bolides in the jet and counterjet. To do this, we fit the displacements of the bolides from the launch point in each epoch assuming simultaneous and oppositely directed launch, followed by ballistic propagation. In Figure 3, each frame has been centred to the estimated launch point, taken to be the gap between the two stationary peaks that correspond to the base of the jets. There are 4 parameters in this model: the proper motions $\mu_{\rm jet}$ and $\mu_{\rm cjt}$, together with the position angle of their trajectories on the sky, and the epoch of launch, $T_{\rm launch}$. That is,

$$\xi_{\alpha,\rm jet} = \mu_{\rm jet}\,(T - T_{\rm launch})\cos\chi\,\sec\delta_0$$
$$\xi_{\delta,\rm jet} = \mu_{\rm jet}\,(T - T_{\rm launch})\sin\chi$$
$$\xi_{\alpha,\rm cjt} = -\mu_{\rm cjt}\,(T - T_{\rm launch})\cos\chi\,\sec\delta_0$$
$$\xi_{\delta,\rm cjt} = -\mu_{\rm cjt}\,(T - T_{\rm launch})\sin\chi$$

where ξ_α and ξ_δ denote shifts in Right Ascension and Declination, the position angle, χ, is the angle formed between the jet and the E-W axis, and δ_0 is the Declination of the source (+4°58′57.″764). We use a least-squares fitting routine, making the simplifiying assumption of uniform, unknown errors in the coordinates. Uncertainties on the fitted parameters are estimated by evaluating the Hessian matrix of second derivatives at the maximum of the posterior PDF, and then using this to approximate the PDF with a multivariate Gaussian.

The fitted proper motions are listed in Table 2 (there are too few data points for a reliable fit to the final ejection, giving a total of 9 fitted bolide pairs). Using equations (2) and (5), the line-of-sight velocity components and the bulk speeds were calculated for each ejecta pair. They are plotted against epoch of launch in Figure 4. The corresponding angles to the line-of-sight are also plotted, showing the precession of the jet launch vector. Uncertainties are estimated by drawing random samples from the Gaussian approximation to the posterior PDF on the fitted parameters, together with the distance to SS 433, $D = 5.5 \pm 0.2$ kpc (Blundell & Bowler (2004)). When propagated through equations (2) and (5), this gives estimates for the errors on the derived parameters. In fact, the uncertainty on distance D is the largest source of uncertainty in the estimation of jet speed β. This is shown in Figure 4(b); we will return to this in Section 5.5.

Inspecting the derived speeds, we see quantitative evidence for a change in behaviour during the campaign. Jet speeds are low ($\beta \lesssim 0.26$) for ejections before approximately day 15. In the later observations, jet speeds are high, exceeding $0.29c$.

5 DISCUSSION

5.1 Do jet speeds and brightnesses rise in flaring episodes?

The 2003 VLBA observations allow us to characterise the distinction between the jets' behaviour in quiescent and flared periods of activity. From Figure 4, we can clearly see the distinct speed distributions before and after day 15: speeds do rise during this flaring episode.

The 2003 VLBA observations make clear that more intensely radiating bolides travel faster than fainter bolides. This is plotted in Figure 5, where peak intensity is plotted against the calculated jet speed for the 9 bolide pairs in the 2003 data whose positions can be securely measured in more than 4 epochs. 'Intensity' here is a representative estimate; it is found by deboosting the total intensity within integrated fitted Gaussians returned by `JMFIT`, averaging over jet and counterjet ejections at each epoch, and then

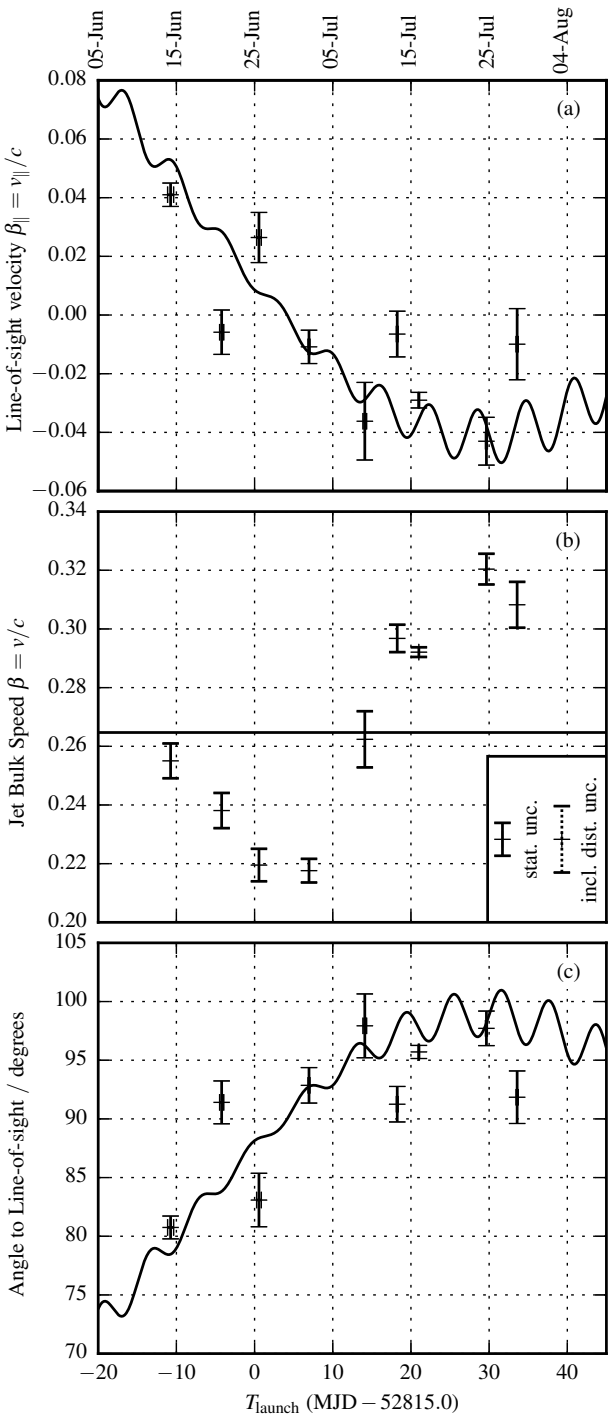

Figure 4. (a) Line-of-sight velocity component, $\beta_\parallel$, plotted against launch date. (b) Jet speed plotted against launch date. (c) Angle between jet bolide velocity vector and line-of-sight. In (a) and (c), the solid line shows the predicted values derived from the kinematic model, while the solid line in (b) shows the value of launch speed derived from optical spectroscopy by Eikenberry et al. (2001): $\beta = 0.2647c$. The systematic deviations from this constant value are clear. Uncertainties shown in (a) and (c) are 1σ. The errorbars in (b) indicate only the uncertainty due to statistical variations in the fitted parameters. We have indicated the effect of the uncertainty in the distance to the object in the inset pane, where the mean statistical uncertainty in the fit (stat. unc.) and mean total uncertainty including that on the distance to SS 433 (incl. dist. unc.) are indicated. See Section 5.5. The errors in launch date are smaller than the marker width on this scale.

Bolide	$T_{\rm launch}$	$\mu_{\rm jet}$/mas d^{-1}	$\mu_{\rm cjt}$/mas d^{-1}	$\beta_\parallel = v_\parallel/c$	$\theta/^\circ$	$\beta = v/c$
1	-10.740 ± 0.385	8.262 ± 0.198	7.611 ± 0.184	0.041 ± 0.004	80.8 ± 1.0	$0.255 \pm (0.006 + 0.005)$
2	-4.211 ± 0.264	7.449 ± 0.209	7.536 ± 0.185	-0.006 ± 0.008	91.4 ± 1.8	$0.238 \pm (0.006 + 0.004)$
3	0.561 ± 0.301	7.046 ± 0.182	6.683 ± 0.192	0.026 ± 0.009	83.1 ± 2.3	$0.220 \pm (0.005 + 0.004)$
4	6.962 ± 0.118	6.768 ± 0.131	6.916 ± 0.133	-0.011 ± 0.006	92.9 ± 1.5	$0.218 \pm (0.004 + 0.005)$
5	14.098 ± 0.231	7.894 ± 0.211	8.487 ± 0.359	-0.036 ± 0.013	97.9 ± 2.7	$0.262 \pm (0.010 + 0.004)$
6	18.247 ± 0.112	9.279 ± 0.141	9.400 ± 0.183	-0.006 ± 0.008	91.3 ± 1.5	$0.297 \pm (0.005 + 0.007)$
7	21.014 ± 0.074	8.891 ± 0.056	9.422 ± 0.058	-0.029 ± 0.003	95.7 ± 0.6	$0.292 \pm (0.002 + 0.009)$
8	29.654 ± 0.126	9.582 ± 0.178	10.443 ± 0.189	-0.043 ± 0.008	97.7 ± 1.5	$0.320 \pm (0.005 + 0.007)$
9	33.583 ± 0.135	9.602 ± 0.269	9.795 ± 0.271	-0.010 ± 0.012	91.8 ± 2.2	$0.308 \pm (0.008 + 0.006)$

Table 2. Best fits to proper motions and bolide launch dates, together with derived line-of-sight velocities $\beta_\parallel$, angles θ to the line-of-sight, and bulk speeds β, for the first 9 bolides seen in the 2003 campaign. $T_{\rm launch}$ is given as MJD − 52815.0 (i.e. referred to 2003-June-25). The bolide numbers correspond to the labels in Figure 3. Uncertainties are at the 1σ level. For the bulk speed, β, the error is given as statistical uncertainty in the fit + systematic uncertainty in the distance D to the source (see discussion in Section 5.5).

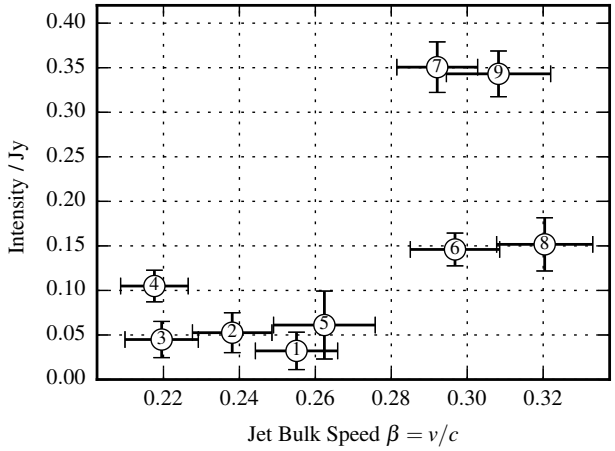

Figure 5. Jet launch speed plotted against intensity for the bolides seen in the 2003 campaign. Intensity is calculated as the peak of the mean of the deboosted intensities for the jet and counterjet. The numbers within the markers denote the bolide's number in the sequence of ejections 2003-Jun-14 to 2003-Jul-28 (see Figure 3 and Table 2).

Bolide	Bulk Speed	Flux on MJD 55919.83 / Jy	
	$\beta = v/c$	Jet	Counterjet
A	0.288 ± 0.017	0.126 ± 0.003	0.095 ± 0.002
B	0.289 ± 0.017	0.518 ± 0.018	0.226 ± 0.008

Table 3. The jet bulk speeds and deboosted fluxes for the two bolide pairs seen in the MJD 55919 (2011-Dec-24) observation. The reported fluxes are integrated fluxes measured using AIPS task `JMFIT`. Note that these fluxes are lower limits for the peak brightness these bolides reach, but that these bolides still obey the "bright-fast" pattern seen for other bolides launched during radio flares (c.f. Figure 5).

selecting the epoch for which this has its maximum value. For details on extracting the true deboosted brightness from a relativistic synchrotron source, see Miller-Jones et al. (2004); here, we have assumed optically thin synchroton emission from a jet composed of discrete plasmons, adiabatically expanding with a constant rate of change of radius, and with electron energy spectrum $\gamma^{-2.2}$, where γ is the electron Lorentz factor (not the bulk Lorentz factor of the jet bolides). It is, however, worth remembering that for SS 433, whose jets are only mildly relativistic and lie close to the plane of the sky, Doppler boosting is a small correction (a few percent, rather than orders of magnitude).

The two 2011 bolides also fit this pattern (Table 3). They are not plotted in Figure 5 because it is not possible to determine their peak brightnesses (since we do not have measurements of the evolution of their lightcurves). However, we can take the averaged and deboosted fluxes from the first of the two observations (MJD 55919, i.e., 2011-Dec-24) observation as lower limits. These bolides' properties (averaged flux densities 0.11 and 0.37 Jy for bolide pairs A and B, with speeds $0.288c$ and $0.289c$ respectively) are consistent with the "bright-fast", flare characteristics displayed by bolides 6, 7, 8, and 9 during the 2003 campaign.

So, the bolides from both the 2003 and 2011 campaigns display a clear trend: *'fast' ejections (those exceeding* $0.28c$*) can be as much as 8 times as luminous as those 'slow' ejections with speeds below* $0.26c$.

Note that not all fast ejections are especially luminous (c.f. bolides 6 and 8). However, in Figure 5, we can again see the separation of the ejections in flaring episodes (bolides 6-9), and those in quiescence (bolides 1-5). This reinforces the conclusion that flaring episodes are characterised by generally faster and more luminous ejections, and that the fastest, most luminous ejections only occur during these periods of elevated activity.

This is entirely consistent with the conclusion of Blundell et al. (2011): high jet speeds as inferred from the *optical* emission lines (which are themselves more intense than usual) precede radio flares. Now, by using only radio maps to infer jet speeds completely independently of optical spectra, we also know that radio flares are characterised by high speeds in the *radio* jets. This further reinforces the link between the optical and radio ejecta.

5.2 How do these data compare with known properties of flares?

Our understanding of this phenomenon has been guided by our association of the behaviour seen on milliarcsecond scales in these maps with the flaring episodes seen in optical spectra and in photometric radio data. In the case of the 2011 data, we can make this comparison slightly more explicit.

It is unfortunate that there are not contemporaneous optical monitoring data for this object covering the periods of these two VLBA campaigns. However, for the 2011 observations, there is monitoring data from the RATAN telescope for the period up to 2011-Dec-15 (Trushkin et al. (2003)). This overlaps with the launch of bolide pair A on 2011-Dec-06. In the total intensity radio data (Figure 6 lower panel), there is evidence that the radio intensity is

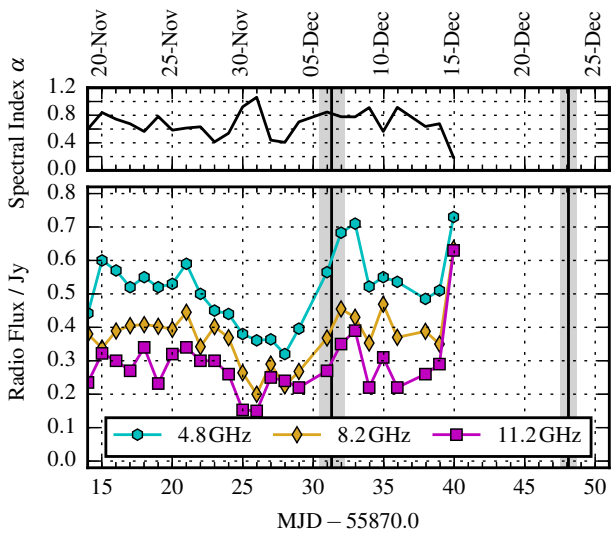

Figure 6. Bottom Panel: Daily radio-frequency fluxes for the period of the 2011 observations, as measured by the RATAN telescope. Top Panel: Corresponding spectral indices, α, for the same period (note that flux $S \propto \nu^{-\alpha}$). The black vertical lines denote the launch dates of the two ejections A and B as calculated in Section 3, with the associated uncertainties in grey.

quenched from 2011-Nov-26, and then rises by perhaps a factor of 3 over the 5 or so days preceding the ejection of bolide pair A (marked by the first grey bar). This pattern fits with the Type II flare described in Blundell et al. (2011), where Type II radio flares were associated with the launch of optical jets. This is the first time that we have seen evidence in SS 433 that a Type II radio flare corresponds to the launch of a radio-emitting jet bolide pair.

As an aside, we emphasise that not all radio flares seen in photometric monitoring are associated with the jets. Type I flares in Blundell et al. (2011) are characterised by a flat spectrum, and are associated with radio emission from an enhanced wind off the accretion disc. The peak in radio intensity at the end of the RATAN monitoring data on 2011-Dec-15 displays a flat radio spectrum, and does not appear to be associated with a bolide launch. 2011-Dec-15 is midway between the launches of bolides A and B – a bolide launched on this date would appear in the gap between these bolides in Figure 2, unless its initial brightness was so faint that it had faded completely before the observation on 2011-Dec-24 (which seems unlikely, given that the peaks in the RATAN data on days 33 and 40 in Figure 6 are of the same size). Consequently, we believe this peak shows the hallmarks of a disc-wind-based radio flare, preceding the launch of a large jet ejection on 2011-Dec-23.

5.3 The circumbinary ruff during radio flares

Several previous VLBI observations of SS 433 have revealed the presence of a circumbinary ruff – an extended region of radio emission aligned above and below the core on the sky, and not associated with the jet (e.g., Paragi et al. (1999), Blundell et al. (2001)). Doolin & Blundell (2009) explored the precession of this ruff using all existing VLBI data – including the observations from 2003 that are shown here in Figure 3. They suggested that the circumbinary ruff is a large scale manifestation of an outflow via a quasi-stable circumbinary disc. This circumbinary disc exists on scales comparable to a few times the orbital separation, and has been observed as static optical emission lines by Blundell et al. (2008)).

We comment that, during the 2003 observations, the ruff appears to grow significantly in size as the flare develops after day 19. We suggest that this may arise from one or more of the following: a) the observed variation is an artefact of changes in *uv*-coverage; b) the ruff appears larger because it is illuminated by more radiation from a brighter, flaring core; or c) the ruff is larger because of enhanced mass outflow from the circumbinary disc. In the first case, we note the apparent dimming of the ruff on days 23 and 26 is suggestive that the effect may be partly artefactual. We also note that the ruff's extent of $\gtrsim 50$ mas is at the upper limit of angular scales to which the VLBA is sensitive, because the shortest VLBA baselines give only sparse coverage of the centre of the *uv*-plane. The third case is intriguing given optical observations of Blundell et al. (2011) that provided evidence that the inner circumbinary disc structure was disrupted during a flare in 2004-October. In the 2003-July observations, there are hints of detatchment between the core components and the radio ruff from day 31 onwards, raising the possibility that the enlarged ruff is a manifestation of an ejected circumbinary disc. However, this would require a very fast outflow speed – at 5.5 kpc, 50 mas corresponds to a physical size of 4×10^{13} m. To cover this in ~ 10 d would require an outflow speed exceeding $40,000\,\mathrm{km\,s^{-1}}$, which seems improbably high (c.f. Miodduszewski et al. (2004)).

5.4 The unified picture

Despite the lack of contemporaneous optical and radio monitoring data, there are enough similarities between what we see in these milliarcsecond scale observations and what is seen at other scales and frequencies that we can draw out some general characteristics.

In Figure 4, we see that jet launch speeds appear to fall over a period of about 30 days before the flare begins and jet speeds increase dramatically on or around day 15. A similar decline in speed is seen in the optical jet lines in figure 6(e) of Blundell et al. (2011), where jet speeds decline from $\sim 0.27c$ to $\sim 0.24c$ over the 20 days prior to a flare.

Both in the 2011-12 observations, and during the latter half of the 2003 campaign, we see bright, fast ejections, punctuated by gaps of 5 to 10 days. Again, almost identical behaviour is seen by Blundell et al. (2011) in the optical jet lines, where the intensity of the optical jet lines is lowest in the days immediately preceding the start of the flare. This stands in contrast to the behaviour of the jet in the early days of the 2003 campaign, where the jet has a more steady character. The difference is most clearly seen by comparing the first and last frame of Figure 3 (noting that the images of all epochs are contoured to the same minimum level): in the first frame we see faint bolides set against an apparently steady background flow, while in the last we see a succession of bright, compact bolides separated by gaps of low/no emission.

Taken together, we note that the variations in both the speeds of the optical emission lines and the speeds determined by the milliarcsecond scale bolides possess remarkably similar characteristics. In the absence of simultaneous, time-resolved optical and radio observations, this coincidence is intriguing evidence that the ejecta revealed by optical emission are indeed directly related to the ejecta seen through radio emission. That is, that both the optical emission lines and the radio continuum emission originate from the same jet moving ballistically and seemingly with the same speed, although this expectation remains to be tested with quasi-simultaneous radio imaging and optical spectroscopy.

5.5 The effect of uncertainty in the distance D

As noted in Section 4, the dominant contribution to the uncertainty in the calculations in Section 2 is the uncertainty in the distance D (c.f. Fender (2003)). For SS 433, we are fortunate to have a well measured distance value, confirmed by two entirely different methods. Firstly, fitting the precession model to the arcsecond-scale radio jets yields a distance of 5.5 ± 0.2 kpc (Blundell & Bowler (2004)). This distance is consistent with the lower limit imposed on the distance by sensitive VLA measurements of HI in absorption at a line-of-sight speed of $75\,\mathrm{km\,s^{-1}}$; absorption at this speed precludes distances for SS433 below 5.5 kpc (Lockman et al. (2007)), assuming the validity of Galactic gas rotation models (Dickey et al. (1983)). Moreover measurements of HI in emission, presented by Lockman et al. (2007) using the Green Bank Telescope, reveal interactions of gas at the same rotation speed (i.e. the same distance) with the W50 nebula that encloses SS 433. Most importantly, since this distance is inferred from HI and Galactic rotation curves, it is totally independent of any assumptions about SS 433's jet speeds; therefore our jet speed determinations on milliarcsecond-scales are not prejudiced by fits to the jet speeds on arcsecond scales. This gives us security in using the distance of Blundell & Bowler (2004).

In the inset panel to Figure 4(b) (and in Table 2), we have indicated the effect of the uncertainty in this distance D. The solid error bars assigned to each data point in the plot show the uncertainties only due to the statistical uncertainty (stat. unc.) in the fits to the proper motions $\mu_{\rm app}$ and $\mu_{\rm rec}$. The dotted error bar in the inset shows the scale of the uncertainties on each speed data point including the distance uncertainty (incl. dist. unc.), i.e., when the distance D is allowed to be drawn from within the range 5.5 ± 0.2 kpc. Since for all measurements, the object must lie at the same distance, the effect of this distance uncertainty is to give a systematic shift in the speed-axis values – the statistical error bars show the uncertainties on each point relative to one another, and give a truer reflection of our confidence that the jet bolides observed in the 2003 campaign show a significant variation in their launch speeds.

The essential point here is that an error in distance measurement would manifest itself as a systematic error in the derived absolute launch speeds across all ejections. It would *not* change our most important overall conclusion: faster jet launch speeds occur during flaring episodes.

6 CONCLUSIONS

The two campaigns of VLBA observations have given us unique measurements of SS 433's radio jet speeds on milliarcsecond scales, and shown that, like their optical counterparts described in Blundell et al. (2011), flaring episodes are associated with faster launch speeds in the radio jets. The 2003 campaign indicates that there may be two quite different types of jet behaviour, namely a flaring mode with a fast, bright jet consisting of compact, discrete ejections, and a quiescent jet consisting of slower bolides set within an apparently more continous background ejection.

Once again, high resolution observations of SS 433 have provided insights into the remarkable complexity of the physics governing the behaviour of microquasars. Contemporaneous observations in optical, radio and X-ray bands are needed to elucidate this further.

ACKNOWLEDGEMENTS

The data for the VLBA movie were reduced by AJM in 2003, and we are pleased to thank Michael Rupen, Craig Walker, and Greg Taylor for helpful discussions about VLBI imaging techniques in relation to these data.

RMJ thanks the Science and Technology Facilities Council for a PhD studentship. This work arose in part from discussions during RMJ's visits to Brandeis University and to NRAO in Socorro and Charlottesville, supported by Merton College, Oxford, and by the Steve Rawlings Memorial Prize. We particularly thank John Wardle, David Roberts, Tony Beasley, Alison Peck, and Rick Perley for sharing their wisdom and insights. We are indebted to Eric Greisen for his help with the finer points of AIPS.

The VLBA is a facility of the National Radio Astronomy Observatory, operated by Associated Universities, Inc., under a cooperative agreement with the National Science Foundation. The figures were produced using the Matplotlib plotting package (Hunter (2007)).

REFERENCES

Abell G. O., Margon B., 1979, Nature, 279, 701
Blundell K. M., Bowler M. G., 2004, ApJ, 616, L159
Blundell K. M., Bowler M. G., 2005, ApJ, 622, L129
Blundell K. M., Mioduszewski A. J., Muxlow T. W. B., Podsiadlowski P., Rupen M. P., 2001, ApJ, 562, L79
Blundell K. M., Bowler M. G., Schmidtobreick L., 2007, A&A, 474, 903
Blundell K. M., Bowler M. G., Schmidtobreick L., 2008, ApJ, 678, L47
Blundell K. M., Schmidtobreick L., Trushkin S., 2011, MNRAS, 417, 2401
Clark J. S., Barnes A. D., Charles P. A., 2007, MNRAS, 380, 263
Dickey J. M., Kulkarni S. R., van Gorkom J. H., Heiles C. E., 1983, ApJS, 53, 591
Doolin S., Blundell K. M., 2009, ApJ, 698, L23
Eikenberry S. S., Cameron P. B., Fierce B. W., Kull D. M., Dror D. H., Houck J. R., Margon B., 2001, ApJ, 561, 1027
Fabrika S., 2004, Astrophysics and Space Physics Reviews, 12, 1
Fender R. P., 2003, MNRAS, 340, 1353
Greisen E. W., 2003, Information Handling in Astronomy - Historical Vistas, 285, 109
Greisen E. W., Spekkens K., van Moorsel G. A., 2009, AJ, 137, 4718
Hjellming R. M., Johnston K. J., 1981, ApJ, 246, L141
Hunter J. D., 2007, Computing In Science & Engineering, 9, 90
Katz J. I., Anderson S. F., Grandi S. A., Margon B., 1982, ApJ, 260, 780
Lockman F. J., Blundell K. M., Goss W. M., 2007, MNRAS, 381, 881
Longair M., 2011, High Energy Astrophysics. Cambridge University Press
Margon B., Anderson S. F., 1989, ApJ, 347, 448
Margon B., Ford H. C., Katz J. I., Kwitter K. B., Ulrich R. K., Stone R. P. S., Klemola A., 1979, ApJ, 230, L41
Marshall H. L., Canizares C. R., Schulz N. S., 2002, ApJ, 564, 941
Miller-Jones J. C. A., Blundell K. M., Duffy P., 2004, ApJ, 603, L21
Mioduszewski A. J., Rupen M. P., Walker R. C., Taylor G. B., 2004, National Radio Astronomy Observatory Press Release, p. 1
Mirabel I. F., Rodríguez L. F., 1994, Nature, 371, 46
NRAO 1990, AIPS Cookbook. National Radio Astronomy Observatory, http://www.aips.nrao.edu/cook.html
Paragi Z., Vermeulen R. C., Fejes I., Schilizzi R. T., Spencer R. E., Stirling A. M., 1999, A&A, 348, 910
Schillemat K., Mioduszewski A., Dhawan V., Rupen M., 2004, in American Astronomical Society Meeting Abstracts. p. 104.01
Trushkin S. A., Bursov N. N., Nizhelskij N. A., 2003, Bulletin of the Special Astrophysics Observatory, 56, 57

This paper has been typeset from a TEX/LATEX file prepared by the author.